

Nonlinear particle acceleration at reverse shocks in supernova remnants

D. C. Ellison¹, A. Decourchelle², and J. Ballet²

¹ Department of Physics, North Carolina State University, Box 8202, Raleigh NC 27695, USA
e-mail: don_ellison@ncsu.edu

² Service d'Astrophysique, DSM/DAPNIA, CEA Saclay, 91191 Gif-sur-Yvette, France
e-mail: [adecourchelle;jballet]@cea.fr

Received 15 July 2004 / Accepted 7 September 2004

Abstract. Without amplification, magnetic fields in expanding ejecta of young supernova remnants (SNRs) will be orders of magnitude below those required to shock accelerate thermal electrons, or ions, to relativistic energies or to produce radio synchrotron emission at the reverse shock. The reported observations of such emission give support to the idea that diffusive shock acceleration (DSA) can amplify magnetic fields by large factors. Furthermore, the uncertain character of the amplification process leaves open the possibility that ejecta fields, while large enough to support radio emission and DSA, may be much lower than typical interstellar medium values. We show that DSA in such low reverse shock fields is extremely nonlinear and efficient in the production of cosmic-ray (CR) ions, although CRs greatly in excess of mc^2 are not produced. These nonlinear effects, which occur at the forward shock as well, are manifested most importantly in shock compression ratios $\gg 4$ and cause the interaction region between the forward and reverse shocks to become narrower, denser, and cooler than would be the case if efficient cosmic-ray production did not occur. The changes in the SNR structure and evolution should be clearly observable, if present, and they convey important information on the nature of DSA and magnetic field amplification with broad astrophysical implications.

Key words. ISM: cosmic rays – acceleration of particles – shock waves – ISM: supernova remnants – X-rays: ISM

1. Introduction

It is clear in many supernova remnants (SNRs) that the forward, blast wave shock, interacting with the interstellar medium (ISM) magnetic field, produces radio (and sometimes X-ray) synchrotron emission. Presumably this is accomplished when the forward shock accelerates thermal and pre-existing cosmic-ray (CR) electrons by diffusive shock acceleration (DSA) (also called the first-order Fermi mechanism). The reverse shock, however, will not produce relativistic electrons from thermal ones if the only magnetic field that is present is the ambient field from the progenitor star. Any progenitor field will be vastly diluted by expansion and flux freezing and, for expected white dwarf or massive star magnetic field values, after < 100 yr, will fall below levels necessary to support particle acceleration to radio emitting energies.

For example, if the surface field of a white dwarf of radius $R_{WD} = 10^7$ m is $B_{WD} = 10^9$ G, the diluted magnetic field after ~ 100 yr at the reverse shock, which is typically at a radius $R_{sk} \sim 1$ pc from the explosion site, is $B \sim B_{WD}(R_{WD}/R_{sk})^2 \sim 10^{-10}$ G. For 10^{-10} G, the diffusive acceleration time to 10 GeV is ≥ 100 yr and the upstream diffusion length at a 10^4 km s⁻¹ shock of a 10 GeV electron is > 1 pc, making the production of radio emitting electrons unlikely. Similar results are

expected for massive progenitors. Furthermore, with such low fields, even if relativistic electrons are present in large numbers from compressed pre-existing cosmic rays or whatever, the radio emissivity may be too low to be observable.

The expanded ejecta bubble may be one of the lowest magnetic field regions in existence and if reverse shocks in some SNRs are accelerating electrons by DSA to radio emitting energies or higher (as has been suggested by recent radio and X-ray observations, e.g., Gotthelf et al. 2001; DeLaney et al. 2002; Rho et al. 2002), there are important consequences for:

- magnetic field generation and amplification in strong shocks;
- the intrinsic efficiency of DSA and cosmic-ray production, including heavy elements; and
- the structure and evolution of the X-ray emitting interaction region between the forward (FS) and reverse shocks (RS).

At the forward shock in some SNRs (see, in particular, Cas A; Vink & Laming 2003), there is convincing evidence for magnetic fields far greater than normal ISM values. It has been suggested that the diffusive shock acceleration process can amplify ambient fields (e.g., Lucek & Bell 2000; Bell & Lucek 2001) to the observed levels, and evidence for this is mounting in specific SNRs, (e.g., Berezhko et al. 2003a,b;

Berezhko & Völk 2004). If such amplification occurs generally, SNRs will be capable of accelerating cosmic rays to above 10^{17} eV (e.g., Ptuskin & Zirakashvili 2003; Drury et al. 2003), possibly solving the decades old problem of smoothly generating CRs to the spectral knee near 10^{15} eV and beyond. Since DSA is expected to occur in diverse environments on all astrophysical scales, the confirmation and characterization of magnetic field amplification is of extreme importance.

In this paper, we first discuss in Sect. 2 the general effects of a low magnetic field on the efficiency of DSA. We show that nonlinear effects, most noticeable in producing compression ratios $\gg 4$, can be extremely large for a range of magnetic field below that of the average ISM (i.e., for $B < B_{\text{ISM}} \sim 3 \times 10^{-6}$ G). We then discuss in Sect. 3 the relevance of low fields and strong nonlinear effects in DSA at reverse shocks in SNRs. To our knowledge, this is the first attempt to consider such effects in an evolutionary model of SNRs. A number of aspects concerning the acceleration process, the nature of the magnetic field, and the physical conditions in the unshocked ejecta material (e.g., temperature, ionization fraction, etc.) are not well-known. Because of these uncertainties, we show a number of examples where important parameters are varied over fairly wide ranges. We emphasize, however, that the effects of efficient DSA on the structure and evolution of SNRs may be large and current instruments should be sensitive enough to importantly constrain many of these poorly known parameters.

2. Nonlinear diffusive shock acceleration

Nonlinear DSA is a complex process that is difficult to describe completely. In order to allow the coupling of the particle acceleration to a hydrodynamic model of SNR evolution, we use an approximate, algebraic model of DSA developed by Berezhko & Ellison (1999) and Ellison et al. (2000). While more complete models exist (e.g., Berezhko et al. 1996), they tend to be more computationally intensive and not as easy to include in a hydrodynamical simulation. Despite the simplifications made in our acceleration model, we believe it adequately describes the essential physics when the maximum momentum of accelerated particles $p_{\text{max}} \gg Am_p c$. It is less accurate when $p_{\text{max}} \sim Am_p c$ as we describe more fully below. Here, A is the mass number, m_p is the proton mass, and c is the speed of light.

In a complicated, nonlinear fashion, the acceleration efficiency (i.e., the fraction of total ram kinetic energy going into superthermal particles)¹ depends on the sonic and Alfvén Mach numbers ($M_S = \sqrt{\rho_0 V_{\text{sk}}^2 / (\gamma P_0)}$ and $M_A = \sqrt{4\pi\rho_0 V_{\text{sk}}^2 / B_0}$ respectively), on the particle injection and on the maximum particle momentum achieved p_{max} . Here, ρ_0 is the unshocked mass density, P_0 is the unshocked pressure, B_0 is the unshocked magnetic field, V_{sk} is the shock speed, and γ is the ratio of specific heats. The particle injection is modeled by two parameters: the injection efficiency η_{inj} , i.e., the fraction of total particles which end up with superthermal energies, and λ_{inj} , which determines the value of the injection momentum ($=\lambda_{\text{inj}} Am_p C_{s2}$,

where C_{s2} is the sound speed in the downstream region). The parameter λ_{inj} , by definition > 1 , is arbitrarily taken to be 4 in our calculations (see Berezhko & Ellison 1999, for a full discussion).

For simplicity, in all our examples we assume a single ion species, generally protons, but in Sect. 4.4, oxygen, with the electron temperature equal to the ion temperature = 10^4 K. We ignore any wave damping from neutral material (see Sect. 5.2.5 below for a discussion). The maximum momentum protons achieve is determined by setting the acceleration time equal to the SNR age t_{SNR} , or by setting the diffusion length of the highest energy particles equal to some fraction, f_{sk} , of the shock radius R_{sk} , whichever gives the lowest p_{max} (see, for example, Baring et al. 1999).

We assume strong turbulence (i.e., Bohm diffusion) so that the scattering mean free path is on the order of the gyroradius, i.e., $\lambda \sim \eta_{\text{mfip}} r_g$, with $\eta_{\text{mfip}} = 1$. The magnetic field strength is thus an important factor in determining p_{max} . If the turbulence is, in fact, weaker than Bohm diffusion ($\eta_{\text{mfip}} > 1$), p_{max} will be smaller for a given background B and the shock compression ratio r_{tot} will be less. Consistent with assuming strong turbulence ($\eta_{\text{mfip}} = 1$), we set, following Völk et al. (2002), the downstream magnetic field $B_2 = \sqrt{1/3 + 2r_{\text{tot}}^2/3} B_0$.²

In the acceleration model of Berezhko & Ellison (1999), the magnetic field also enters in a calculation of the transfer of energy from energetic particles to the background gas via Alfvén waves, i.e.,

$$\frac{u\rho^\gamma}{(\gamma-1)} \frac{\partial}{\partial x} (P_{\text{gas}}\rho^{-\gamma}) = V_A \frac{\partial P_{\text{CR}}}{\partial x}, \quad (1)$$

where $V_A = B/\sqrt{4\pi\rho}$ is the Alfvén velocity, u is the flow speed, P_{gas} is the pressure in the background gas, and P_{CR} is the pressure in the relativistic particles, i.e., cosmic rays. It is implicitly assumed that the turbulence saturates when $\delta B/B \sim 1$ and the wave energy is then rapidly damped to heat. Thus, magnetic field amplification is not included in this description.

It is via this energy transfer from energetic particles that the magnetic field has its largest effect on the acceleration process and even small amounts of background heating from the damping of Alfvén waves can significantly reduce the acceleration efficiency compared to the case where only adiabatic heating is included.

As explained in detail in Berezhko & Ellison (1999), compression ratios > 4 occur in DSA for two reasons. First, as relativistic particles are produced and contribute significantly to the total pressure, their softer equation of state makes the shocked plasma more compressible (as $\gamma \rightarrow 4/3$, $r_{\text{tot}} \rightarrow 7$). Second, as the highest energy particles escape from the shock, they drain away energy flux which must be compensated for by ramping up the overall compression ratio to conserve the fluxes. Just as in radiative shocks, this is equivalent to $\gamma \rightarrow 1$ and r_{tot} can become arbitrarily large. Compression ratios as large as we show here occur in independent steady-state calculations of nonlinear DSA which account for particle loss (e.g., Eichler 1984;

¹ Note the difference between injection efficiency η_{inj} and acceleration efficiency. The acceleration efficiency can and does vary with shock parameters even for a constant η_{inj} .

² Everywhere, the subscript 0 (2) implies unshocked (shocked) quantities.

Jones & Ellison 1991; Malkov 1998; Blasi 2002). We note that as the overall compression ratio increases ($r_{\text{tot}} > 4$), the subshock compression ratio, r_{sub} , which is responsible for heating the gas, becomes less than the test-particle value ($r_{\text{sub}} < 4$), causing the temperature of the shocked gas to drop below test-particle values.

Two important qualifications must be made concerning particle escape and the production of compression ratios greater than 7. First, the explicit assumption in the model of Berezhko and Ellison (and the others mentioned above) is that steady-state conditions apply and particle acceleration is terminated as particles diffuse away from the shock. If, instead, the acceleration time becomes comparable to the shock age while the diffusion length is still a small fraction of the shock radius, the acceleration process may terminate without particle escape (e.g., Drury 1983). It is less clear what happens in this case, although the work of Berezhko and co-workers (e.g., Berezhko 1996; Berezhko et al. 1996) suggests that for the forward shock in SNRs, geometrical factors determine p_{max} over most of the lifetime. These geometrical factors, i.e., the diffusion of particles upstream from the shock, the increase in the shock size and upstream volume, the slowing of the shock speed, and the adiabatic cooling of the energetic particles, produce effects similar to those from escaping particles even though particles, in fact, remain in the SNR system (see a comparison of the modeling of SN1006 using the simple, steady-state model used here with the time-dependent model of Berezhko and co-workers in Ellison et al. 2000).

The situation is more uncertain for the inward facing, reverse shock since the upstream region has a finite volume and particles streaming far upstream can conceivably reach the shock on the opposite side of the explosion site without being lost. In this case, particles may still be lost from spatial effects if they diffuse far enough downstream to reach the contact discontinuity. However, large magnetic fields are expected at the contact discontinuity due to compression and stretching of the field lines by Rayleigh-Taylor instabilities, and might act as a magnetic wall confining the particles in the ejecta material.

In any case, for either the forward or reverse shock, a precise determination of the compression ratio in a time-dependent situation requires a detailed knowledge of the wave-particle interactions in the self-generated magnetic turbulence responsible for particle diffusion. This knowledge does not yet exist so approximations remain necessary. We simply assume that particles at either the forward or reverse shock leave the system when their acceleration time $> t_{\text{SNR}}$ or their upstream diffusion length $> f_{\text{sk}} R_{\text{sk}}$. In all of the SNR models we show in this paper, we arbitrarily take $f_{\text{sk}} = 0.05$ and note that p_{max} and r_{tot} would increase with increasing f_{sk} .

The second qualification is that the approximations in the Berezhko and Ellison model assume that $p_{\text{max}} \gg Am_p c$ and thus, that a sizable fraction of the total pressure is in relativistic particles. Despite this limitation, we show cases where $p_{\text{max}} \gtrsim 2Am_p c$ and warn that our lower p_{max} results have a greater intrinsic error than those with $p_{\text{max}} \gg Am_p c$. In fact, from comparisons with Monte Carlo results (not shown here), we find that the Berezhko and Ellison model underestimates r_{tot} when $p_{\text{max}} \sim Am_p c$.

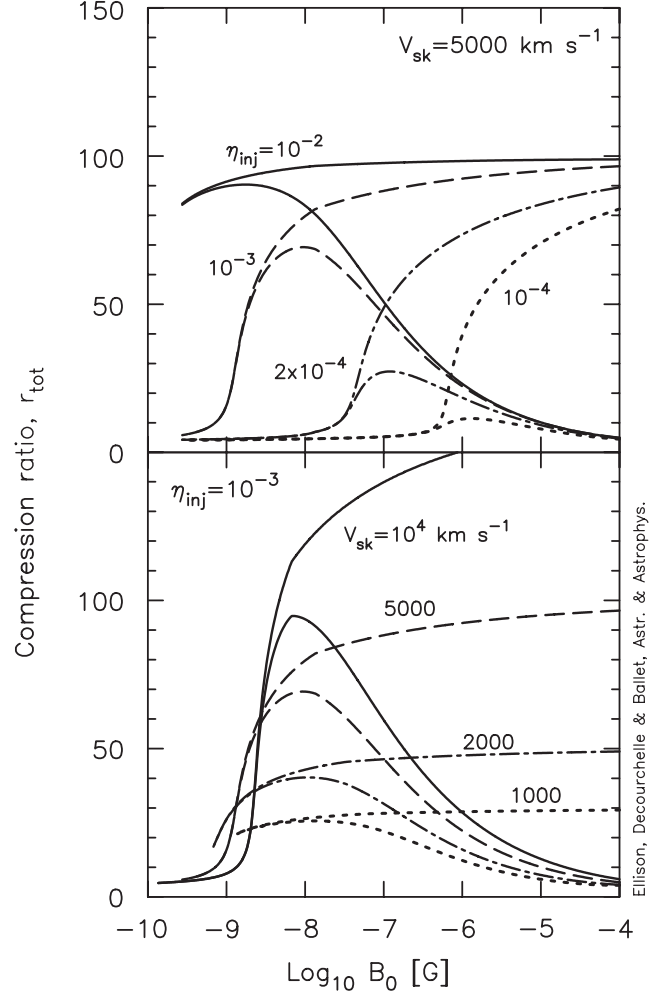


Fig. 1. Compression ratio versus unshocked magnetic field for a constant shock speed V_{sk} and different values of the injection efficiency η_{inj} (top panel), and for a constant injection efficiency and different values of the shock velocity (bottom panel). For each set of parameters, the upper curve corresponds to adiabatic heating in the precursor and the lower one to Alfvén-wave heating in the precursor. In the latter case, r_{tot} is dramatically reduced as B_0 increases.

3. Efficient diffusive shock acceleration in weak magnetic fields

In this section, we investigate how the acceleration efficiency depends on the upstream magnetic field B_0 for a fixed set of parameters; R_{sk} , f_{sk} , t_{SNR} , and proton number density n_p . We chose a value of t_{SNR} large enough to ensure that p_{max} is determined by diffusive escape. In this case, since we set $\eta_{\text{mfp}} = 1$ and R_{sk} and f_{sk} are fixed, p_{max} depends only on B_0 and V_{sk} :

$$p_{\text{max}} \simeq 3Ze f_{\text{sk}} R_{\text{sk}} B_0 V_{\text{sk}} / c, \quad (2)$$

where Z is the charge number or ionization state and e is the electronic charge.

Figure 1 shows the variation of the overall shock compression ratio r_{tot} versus magnetic field (top panel) for different values of the injection parameter η_{inj} with V_{sk} set to 5000 km s^{-1} and (bottom panel) for different values of the shock velocity with η_{inj} set to 10^{-3} . In both panels, $R_{\text{sk}} = 3 \text{ pc}$, $t_{\text{SNR}} = 1200 \text{ yr}$,

$n_p = 0.3 \text{ cm}^{-3}$, and the plasma is composed of protons and electrons only.

Each value of η_{inj} has two curves, one with only adiabatic heating in the precursor and one with Alfvén-wave heating in the precursor. The transfer of energy from the energetic particles to the background gas via Alfvén waves reduces r_{tot} dramatically as B_0 increases. With Alfvén-wave heating, very large compression ratios are obtained only for values of the magnetic field much lower than that typical of the interstellar medium (i.e., for $B_0 \ll 3 \times 10^{-6} \text{ G}$). This compression ratio increases with decreasing magnetic field up to a maximum, whose position and intensity depend on the injection parameter, and then decreases to the test-particle value of 4.

In the top panel, the sonic Mach number is fixed and the only relevant varying parameters are p_{max} and the Alfvén Mach number, M_A . As B_0 decreases, p_{max} decreases and M_A increases. For $B_0 \gtrsim 2 \times 10^{-8} \text{ G}$, the magnetic field is strong enough to allow a significant transfer of energetic particle energy through Alfvén waves to heat, lowering the acceleration efficiency. The greater B_0 , the smaller M_A and the more important this effect becomes, causing $r_{\text{tot}} \rightarrow 4$. For $B_0 \lesssim 2 \times 10^{-8} \text{ G}$, M_A is large enough that it is no longer important, but now p_{max} becomes small enough that the fraction of pressure in relativistic particles drops below that required to maintain a strongly modified shock. As B_0 decreases, the transition from a strongly modified shock with $r_{\text{tot}} \gg 4$ to an *unmodified* one with $r_{\text{tot}} \sim 4$ occurs and can be extremely abrupt. As explained in Berezhko & Ellison (1999), the larger η_{inj} is, the more difficult it is to have a high-Mach number, unmodified solution. This is the reason that the maximum value of the compression ratio increases, and that the position of the maximum shifts towards lower B_0 , as η_{inj} increases.

In the bottom panel, both M_S and M_A vary. With Alfvén-wave heating, as B_0 decreases, the curves for $V_{\text{sk}} = 1000$ and 2000 km s^{-1} end before the compression ratio drops to 4: in these cases, p_{max} becomes low enough ($\lesssim 2 m_p c$) to invalidate the approximations of the Berezhko and Ellison model.

As B_0 increases and M_A drops, the damping effects of the magnetic field increase and cause r_{tot} to drop toward 4, regardless of the sonic Mach number. For values of magnetic field near 10^{-8} G in the Alfvén-wave heating curves, the compression ratio peaks strongly as the shock velocity and, therefore, M_S increase. As B_0 decreases below $\sim 10^{-8} \text{ G}$, the lowering of p_{max} , and subsequent reduction of pressure in relativistic particles, causes the transition to unmodified solutions regardless of M_S . The magnetic field where r_{tot} is a maximum shifts slightly toward lower B_0 as M_S increases. Using the Berezhko and Ellison model, an approximate expression for the magnetic field strength, B_* , at the transition point between unmodified and strongly modified solutions can be derived in two regimes (for $p_{\text{max}} \leq$ or $> 100 Am_p c$):

$$B_* \simeq \frac{(x_1 / \sqrt{10})^4}{x_2} \frac{V_{\text{sk}}^3}{\eta_{\text{inj}}^4 c^2} \quad (3)$$

if $p_{\text{max}} > 100 Am_p c$,

or

$$B_* \simeq \frac{x_1^2 V_{\text{sk}}}{x_2 \eta_{\text{inj}}^2} \quad (4)$$

if $p_{\text{max}} < 100 Am_p c$,
where

$$x_1 = \frac{r_{\text{sub}} - 1}{2\lambda_{\text{inj}} \sqrt{r_{\text{sub}}}} \times \frac{\sqrt{\gamma + 1}}{\sqrt{2\gamma - \frac{\gamma-1}{M_S^2} (r_{\text{tot}}/r_{\text{sub}})^{\gamma+1}}} \quad (5)$$

$$x_2 = \frac{3f_{\text{sk}} Z e R_{\text{sk}}}{A \eta_{\text{mfip}} m_p} \quad (6)$$

At the transition, r_{tot} can be estimated as $0.65 M_S^{3/4}$ and $r_{\text{sub}} = 4$ (Berezhko & Ellison 1999). The break at $100 Am_p c$ mirrors the break in the Berezhko and Ellison model between a three-component power law when $p_{\text{max}} \geq 100 Am_p c$ and a two-component power law when $p_{\text{max}} < 100 Am_p c$.

Figure 1 illustrates that even if extremely high compression ratios are theoretically possible, normal ISM magnetic field values, i.e., $B_{\text{ISM}} \gtrsim 3 \times 10^{-6} \text{ G}$, with Alfvén-wave heating, are sufficiently high to limit compression ratios to $r_{\text{tot}} \lesssim 20$, regardless of how efficient the injection is or how high the sonic Mach number is. The energy converted to magnetic turbulence and heat lowers the subshock Mach number and the overall acceleration efficiency. Also, when M_A is low, the speed of the magnetic scattering centers in the fluid (assumed to be Alfvén waves) can become comparable to the shock speed, lowering the effective difference (for acceleration) between the downstream and upstream flow speeds³. The low magnetic fields in expanding supernova ejecta offer a unique possibility of seeing non-radiative shocks with $r_{\text{tot}} \gtrsim 20$.

4. Particle acceleration at reverse shocks in SNRs

4.1. Assumptions and parameters for the CR-hydro simulation

We model the effects of cosmic-ray acceleration on the evolution of a SNR using a one-dimensional, cosmic-ray hydrodynamic (CR-hydro) simulation as described in Ellison et al. (2004).

We initialize the CR-hydro simulation at some time t_0 after the explosion with a power-law ejecta density distribution, $\rho_{\text{ej}} \propto r^{-n}$ (of index $n = 7$), combined with a constant density plateau region at small radii. The plateau is required to keep the total ejecta mass finite. Beyond the ejecta, we assume a uniform ISM mass density $\rho_{\text{ISM}} = 5 \times 10^{-25} \text{ g cm}^{-3}$ corresponding to a proton number density of 0.3 cm^{-3} . A constant density ISM is more appropriate for a type Ia supernova, whereas a type II supernova is likely to explode in a pre-SN stellar wind with a $\rho \propto r^{-2}$ density structure. The presence of a stellar wind will affect the density and temperature structure of the shocked ejecta

³ Note that even though we consider cases where the speed of the scattering centers is high, we neglect second-order Fermi acceleration.

and this, in turn, will change the quantitative aspects of particle acceleration at the reverse shock. Qualitatively, however, the effects we describe for a uniform ISM will be present in type II supernovae as well.

The hydrodynamical simulation only recognizes the matter density, but the acceleration model depends on the ion species and is limited to a single species, as we discuss below. We assume that the ejecta speed varies linearly with radius from zero to some maximum speed V_{\max}^{ej} . In the simulation, the initial maximum radius of the ejecta is set by the maximum ejecta speed and t_0 . Thus, the early stages of the simulation will depend on V_{\max}^{ej} and t_0 . As long as the total kinetic energy and ejecta mass stay the same, however, the later evolution of the SNR is independent of both V_{\max}^{ej} and t_0 .

In Fig. 2 we show how the early evolution depends on V_{\max}^{ej} for a particular set of SNR parameters. For all of our other examples, except those indicated in Fig. 2, we take $V_{\max}^{\text{ej}} = 3 \times 10^4 \text{ km s}^{-1} \approx 0.1c$. As long as t_0 is earlier than the time when p_{\max} becomes greater than $2 Am_p c$, as is the case in Fig. 2, our results are independent of t_0 .

For comparison, we also show in Fig. 2 (dot-dashed curve) the results obtained analytically for the same set of parameters using modified Chevalier solutions (Decourchelle et al. 2000). Good agreement is reached after a few tens of years and, in fact, all of our simulation results, after a few decades, are independent of our starting conditions and consistent with analytic solutions, as long as the self-similar conditions required for the analytic solutions are valid.

4.2. Constant ejecta magnetic field

Given the general behavior of DSA in low magnetic fields, we begin our study of SNRs by assuming a constant ejecta magnetic field upstream from the reverse shock.

For the CR-hydro model, we use the following parameters: supernova explosion kinetic energy $E_{\text{SN}} = 10^{51}$ erg, ejecta mass $M_{\text{ej}} = 1.4 M_{\odot}$, and $B_{\text{ISM}} = 3 \times 10^{-6}$ G for the upstream ISM field (this is B_0 for the forward shock). For the acceleration calculation, we take $\eta_{\text{inj}} = 10^{-3}$ here and in all following models for both the forward and reverse shocks⁴.

The top panel of Fig. 3 shows the variation of the compression ratio with SNR age for different values of the constant upstream ejecta magnetic field B_{ej} (B_0 for the reverse shock). For $B_{\text{ej}} \geq 3 \times 10^{-6}$ G, the compression ratio is smaller than 20 for a SNR age larger than 100 yr. For $B_{\text{ej}} \leq 3 \times 10^{-7}$ G, however, the reverse shock compression can be extremely high: $r_{\text{tot}} \sim 60$ at $t_{\text{SNR}} \sim 100$ yr for $B_{\text{ej}} = 3 \times 10^{-8}$ G (dashed curve). The analytical results for $B_{\text{ej}} = 3 \times 10^{-7}$ G are shown as long-dashed curves in the top two panels. As explained for Fig. 2, the early evolution depends on V_{\max}^{ej} but good agreement is obtained for higher V_{\max}^{ej} or, in any case, after ~ 10 yr. The change in the slope in the simulation curves at ~ 400 yr corresponds to the

⁴ In an actual SNR, of course, the injection efficiency might vary with time, vary over the shock surface, or be different at the forward and reverse shocks (as in our model of Kepler's SNR; Decourchelle et al. 2000). If the actual η_{inj} is less than 10^{-3} , the nonlinear effects we show will be less dramatic.

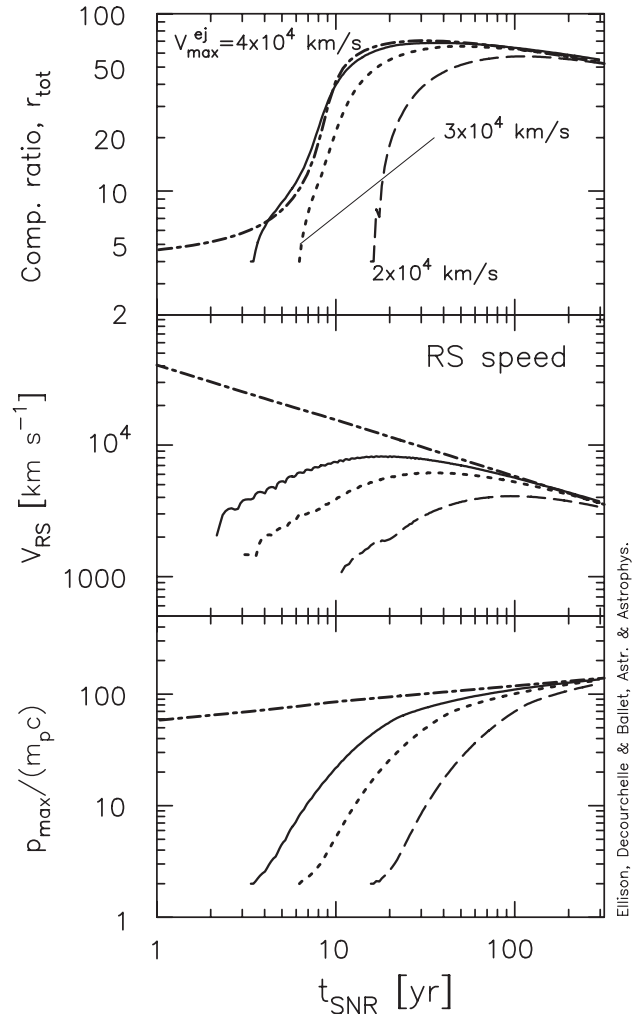


Fig. 2. All curves are for the reverse shock and use the same set of parameters with a constant magnetic field $B_{\text{ej}} = 3 \times 10^{-8}$ G. The only variable is the maximum speed of the ejecta V_{\max}^{ej} which is $4 \times 10^4 \text{ km s}^{-1}$ for the solid curves, $3 \times 10^4 \text{ km s}^{-1}$ for the dotted curves, and $2 \times 10^4 \text{ km s}^{-1}$ for the dashed curves. For comparison, we show the results obtained analytically, where V_{\max}^{ej} is not limited, for the same set of parameters using modified Chevalier solutions. While all curves converge after several decades, the early evolution depends on the different hydrodynamic initial conditions. The simulation curves are truncated when $p_{\max} < 2m_p c$.

passage of the reverse shock from the power-law envelope into the plateau. Such a transition is not included in the analytic result which is only valid while the reverse shock remains in the power-law profile.

Lowering B_{ej} causes the particle gyroradius and acceleration time to increase so in a shock of a given size and age, p_{\max} decreases, as seen in the middle panel of Fig. 3. Below some minimum value, B_{ej} will be too weak to allow the acceleration of particles to radio emitting energies. This opens up the possibility that a range of B_{ej} may exist greater than the minimum value needed to produce observable radio emission

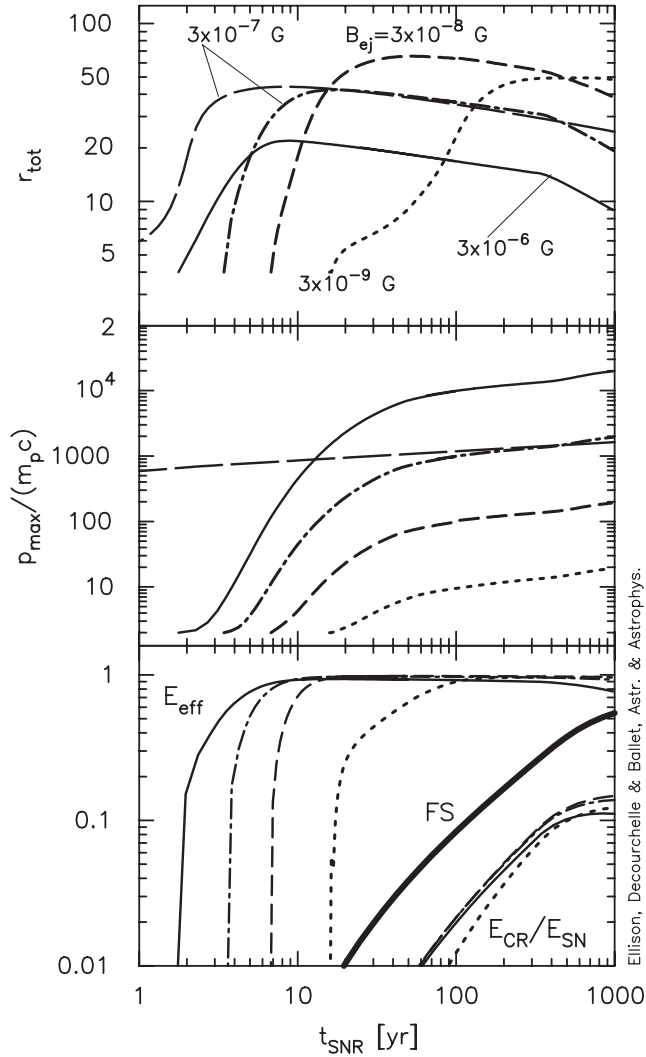


Fig. 3. In each panel, RS results are shown for $B_{ej} = 3 \times 10^{-6}$ G (solid curves), 3×10^{-7} G (dot-dashed curves), 3×10^{-8} G (dashed curves), and 3×10^{-9} G (dotted curves). The long-dashed curves in the top and middle panels are analytic results with $B_{ej} = 3 \times 10^{-7}$ G. In the bottom panel, E_{eff} is the RS acceleration efficiency and E_{CR}/E_{SN} is the fraction of SN explosion energy going into CRs. The curve labeled “FS” is E_{CR}/E_{SN} for the FS (FS results are insensitive to B_{ej}). In all cases, $B_{ISM} = 3 \times 10^{-6}$ G and curves are truncated when $p_{max} < 2m_p c$.

but less than $\sim 3 \times 10^{-6}$ G so that the full nonlinear effects of efficient Fermi acceleration of ions occurs⁵.

The efficiency of the DSA process can be extremely high. In the bottom panel of Fig. 3 we show the instantaneous acceleration efficiency E_{eff} , defined as the fraction of incoming energy flux (in the shock rest frame) put into relativistic particles. After a few decades, all of the models show $E_{eff} \gtrsim 0.9$. The curves in the bottom panel on the right show the fraction of the supernova explosion energy E_{SN} put into relativistic particles, i.e., E_{CR}/E_{SN} . The reverse shocks are able to put $\sim 10\%$ of E_{SN} into CRs after 1000 yr. The forward shocks put $\sim 50\%$

⁵ Note that we do not show solutions in Fig. 3 for $p_{max} < 2m_p c$, i.e., below the limit of validity of the Berezhko and Ellison model.

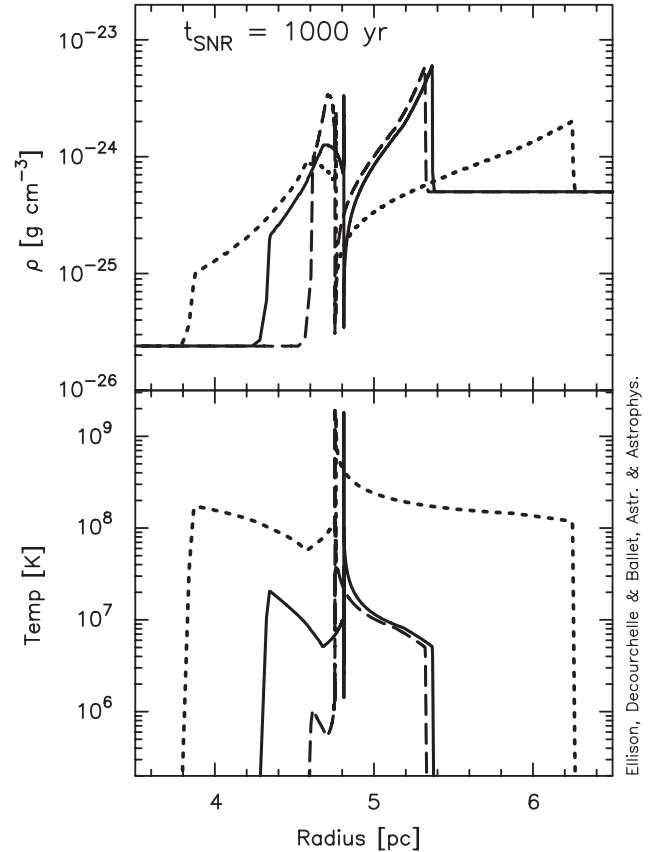


Fig. 4. The top panel shows the plasma density vs. radius and the bottom panel shows the temperature vs. radius. In both panels, the solid curves include the effects of efficient DSA with a constant ejecta magnetic field $B_{ej} = 3 \times 10^{-6}$ G, the dashed curves assume $B_{ej} = 3 \times 10^{-8}$ G, and the dotted curves are results with no acceleration (i.e., test-particle). In all cases the results are calculated at $t_{SNR} = 1000$ yr with $B_{ISM} = 3 \times 10^{-6}$ G.

of E_{SN} into CRs, as shown by the heavy-weight solid curve labeled “FS”⁶.

In the strong nonlinear regime, radical changes in the structure of the interaction region between the forward and reverse shocks occur. In Fig. 4 we compare nonlinear density and temperature profiles with $B_{ej} = 3 \times 10^{-6}$ G (solid curves) and $B_{ej} = 3 \times 10^{-8}$ G (dashed curves) against profiles obtained with no acceleration (dotted curves). All of the profiles are plotted at $t_{SNR} = 1000$ yr. In the cases with efficient particle acceleration, the increased compression ratios make the interaction region narrower, denser, and cooler than with no acceleration. This is particularly true for the width of the shocked ejecta region which, compared to the case with no acceleration, shrinks by a factor of ~ 5 when $B_{ej} = 3 \times 10^{-8}$ G and where the temperature drops from greater than 10^8 K to $\sim 10^6$ K.

⁶ As noted by Berezhko et al. (2002), injection may vary over the surface of the SNR and be significantly less where the magnetic field is highly oblique. They estimate that to supply the galactic CR population the overall efficiency need only be $\sim 20\%$ of the maximum values obtained by DSA.

Note that the density and temperature profiles drop abruptly with no apparent precursors (the small precursors seen in Figs. 4 and 6 below, are numerical from a finite grid). This is because our current CR-hydro model does not explicitly include the cosmic-ray precursor in the hydrodynamics. The precursor effects essential for the nonlinear acceleration (i.e., shock smoothing and pre-heating) are included in the particle acceleration model. For the solid curves in Fig. 4, the upstream density precursor at the reverse shock would be ~ 0.2 pc in extent to be consistent with our assumption that $f_{\text{sk}}R_{\text{sk}}$ sets the upstream diffusion length of particles of momentum p_{max} . We further note that regardless of the density precursor, a precursor in thermal X-rays is not expected because the temperature in the precursor is too low. The nonthermal X-ray precursor will be much narrower than the density precursor if the electron spectrum is limited by cooling, as suggested by the narrow width of the filaments.

The changes in structure and evolution of the SNR brought about by efficient DSA are so large that, even considering the difficulties projection effects present and other uncertainties, they should be observable with current techniques. On the other hand, if radio emission is unambiguously observed at reverse shocks without such dramatic structural changes, this would be evidence for either magnetic field amplification beyond several μG , or that DSA doesn't produce large compression ratios as the theory with particle escape predicts, or that the injection rate is considerably lower than the value $\eta_{\text{inj}} = 10^{-3}$ we have assumed.

4.3. Non-uniform, diluted ejecta field

The structure of the magnetic field in SNR ejecta is clearly more complex than assumed in the previous section. As the ejecta expands, the conservation of magnetic flux will cause the field strength to decrease rapidly and after only a few years, B_{ej} may fall below the 3×10^{-8} G value used in Fig. 3. The highest possible initial values of the magnetic field are expected for white dwarf (WD) progenitors of type Ia supernovae and range between 10^5 and 10^9 G (e.g., Liebert 1995). Further enhancement of the WD magnetic field by convection effects could occur prior to explosion during the phase of quasi-static burning of carbon and could possibly lead to equipartition between the kinetic energy density and magnetic field density. If this occurs, fields as high as 10^{10} – 10^{11} G might result (e.g., Ruiz-Lapuente & Spruit 1998), providing the upper limit on the initial magnetic field intensity we consider in the following.

After the explosion of the progenitor, the rapid expansion of the ejecta will dilute the magnetic field. We obtain expressions for the magnetic field at time, t , in the core (i.e., the plateau region) of the ejecta B_{core} , and in the outer, power-law part of the ejecta B_{PL} , as a function of fluid speed V , by assuming that the magnetic field is initially uniform in a constant density progenitor and then carried passively over during the explosion with the magnetic flux being conserved during the expansion. Therefore,

$$B_{\text{core}} = B_{\text{WD}} \left(\frac{V_{\text{ej}} t}{R_a} \right)^{-2} \quad (7)$$

$$B_{\text{PL}} = B_{\text{core}} \left(\frac{V}{V_{\text{ej}}} \right)^{-2} \times \left[1 + \frac{3}{n-3} \left(1 - \left(\frac{V}{V_{\text{ej}}} \right)^{3-n} \right) \right]^{\frac{2}{5}}. \quad (8)$$

Here, B_{WD} is the magnetic field in the white dwarf before the explosion, V_{ej} is the constant fluid velocity at the core-power-law transition point, R_a is the radius within the white dwarf enclosing the mass of what will become the core of the ejecta, and n is the ejecta density power-law index. Given $V_{\text{max}}^{\text{ej}}$, E_{SN} and t_0 , V_{ej} is obtained numerically in the hydro simulation and

$$R_a = R_{\text{WD}} \left[\frac{n-3}{n-3(V_{\text{max}}^{\text{ej}}/V_{\text{ej}})^{3-n}} \right]^{1/3}, \quad (9)$$

where R_{WD} is the white dwarf radius before the explosion.

Despite specifying white dwarf parameters in the above equations, similar behavior is expected for the ejecta in type II supernovae but starting with a lower magnetic field at a larger radius. Basically, any pre-SN field will be diluted by the expanding ejecta such that $B_{\text{ej}} \propto R^{-2}$.

In Fig. 5, we show the variations of r_{tot} , p_{max} , and ν_c versus t_{SNR} for a diluted field B_0 , as defined by Eqs. (7) and (8). The frequency ν_c is the critical frequency (e.g., Rybicki & Lightman 1979) where synchrotron emission from an electron of p_{max} peaks, i.e.,

$$\nu_c = 3p_{\text{max}}^2 eB / [4\pi(m_e c)^3]. \quad (10)$$

Here m_e is the electron mass and we have taken the sine of the pitch angle = 1 for convenience.

The solid curves in Fig. 5 show the extreme case with $B_{\text{WD}} = 10^{11}$ G. In this case, the ability of the reverse shock to produce ~ 10 GeV particles lasts until $t_{\text{SNR}} \sim 50$ yr, after which B_0 drops below $\sim 10^{-8}$ G. The dashed curves show results for $B_{\text{WD}} = 3 \times 10^{10}$ G. Despite B_{WD} being as high as 3×10^{10} G, few GeV particles are produced at the RS. This is contrasted by the FS (dot-dashed curves) where $> 10^4 m_p c$ particles are produced after ~ 100 yr.

Even though the maximum momenta produced in these diluted magnetic field examples are low, large structural changes occur early in the evolution, as shown in Fig. 6, where the density and temperature profiles are plotted at $t_{\text{SNR}} = 100$ yr. The differences between the test-particle case (dotted curves) and the efficient acceleration cases (solid and dashed curves) are greater for the forward shocks, but are substantial at the reverse shocks. The structure changes at the reverse shocks lessen as t_{SNR} becomes greater than 100 yr.

In Fig. 7 we show the reverse shock synchrotron emission predicted for the $B_{\text{WD}} = 3 \times 10^{10}$ and 10^{11} G examples shown in Fig. 5, along with emission from the forward and reverse shocks where B_{ej} is held constant at 3×10^{-6} G and 3×10^{-8} G as labeled. For calculating synchrotron emission here and elsewhere, we assume the electron to proton density ratio at relativistic energies to be 0.01, similar to that observed for galactic cosmic rays (see Baring et al. 1999; Ellison et al. 2000, for discussions of how electrons are treated and synchrotron emission calculated in this model). These curves are calculated at

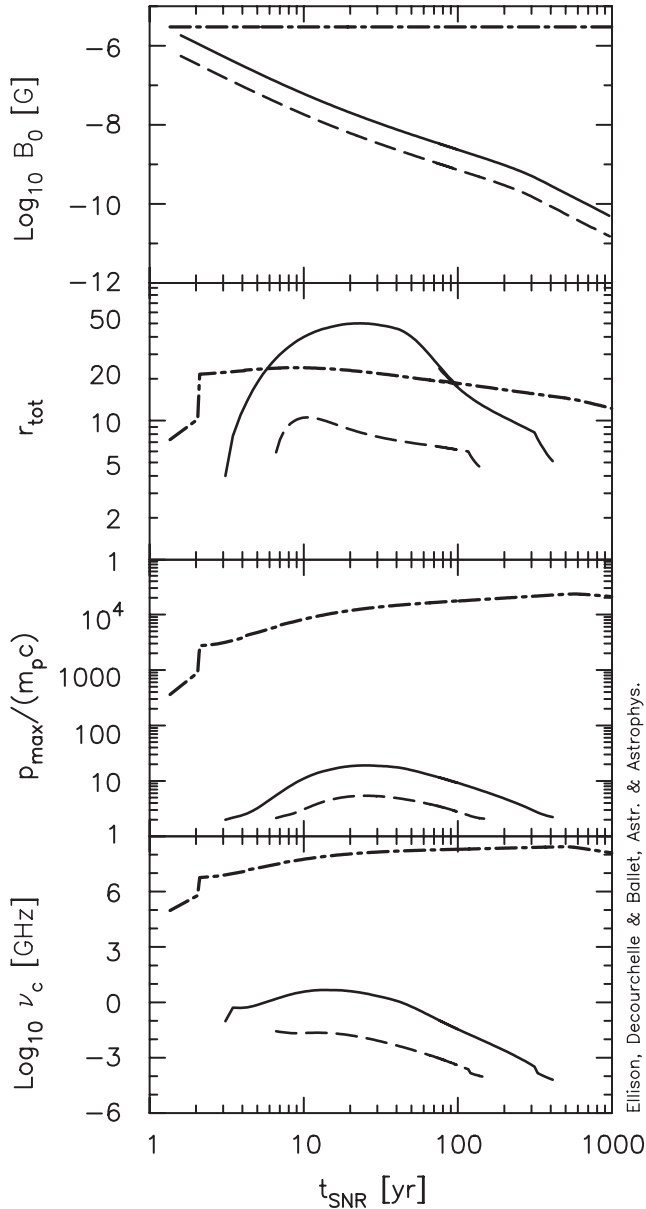


Fig. 5. Results from two models with diluted magnetic fields are shown. In all panels, the solid curves are RS values with $B_{\text{WD}} = 10^{11}$ G, the dashed curves are RS values with $B_{\text{WD}} = 3 \times 10^{10}$ G, and the dot-dashed curves are FS values, which are insensitive to B_{WD} . For both models, $B_{\text{ISM}} = 3 \times 10^{-6}$ G and only values where $p_{\text{max}} > 2 m_p c$ are plotted.

$t_{\text{SNR}} = 1000$ yr at a distance of 2 kpc, typical of SN1006. At 1 GHz radio frequencies, the reverse shock emission from even the most extreme white dwarf case with dilution falls more than 5 orders of magnitude below that of the forward shock⁷. For the constant $B_{\text{ej}} = 3 \times 10^{-8}$ G case, the reverse shock emission is about a factor of 100 below the reverse shock emission with $B_{\text{ej}} = 3 \times 10^{-6}$ G at 1 GHz. Note that the 3×10^{-8} G field is too weak to produce X-ray synchrotron emission as reported for SNR RCW 86 (Rho et al. 2002).

⁷ The properties of the forward shock are quite insensitive to the ejecta magnetic field so each of these four models have similar forward shock synchrotron emission.

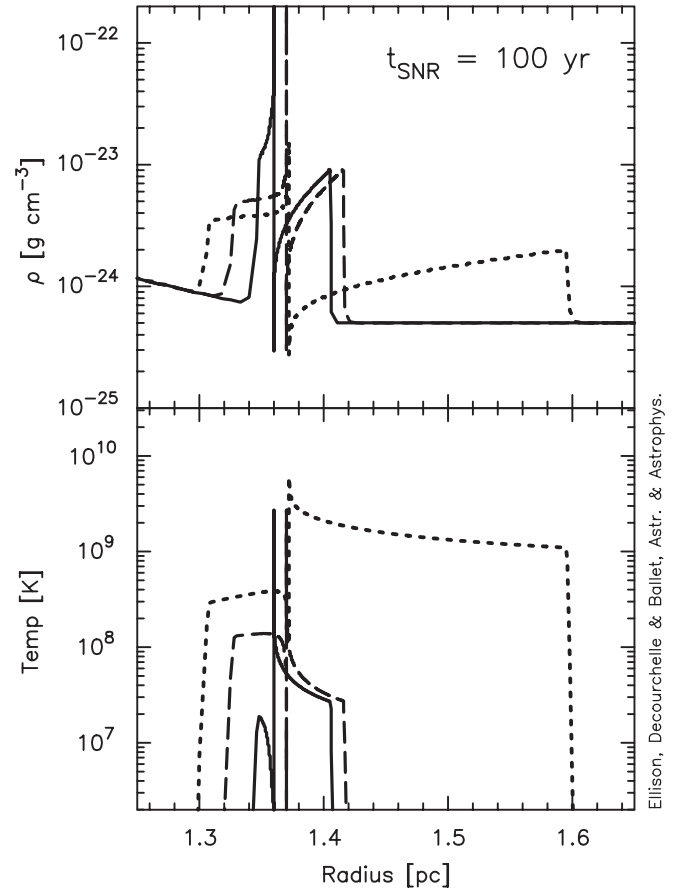


Fig. 6. This figure shows the density and temperature profiles with diluted ejecta fields. The dotted curves are results with no shock acceleration, the solid curves are results with $B_{\text{WD}} = 10^{11}$ G, and the dashed curves are results with $B_{\text{WD}} = 3 \times 10^{10}$ G.

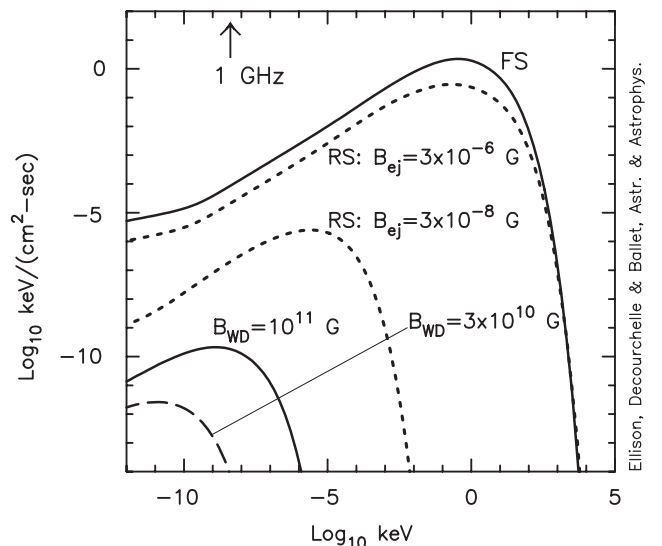


Fig. 7. Integrated synchrotron emission for constant and diluted ejecta magnetic fields at $t_{\text{SNR}} = 1000$ yr. The upper three curves are calculated assuming a constant field $B_0 = 3 \times 10^{-6}$ G upstream of the forward shock and constant B_{ej} as labeled. The solid and dashed curves are the emission from the reverse shock assuming a diluted white dwarf field of $B_{\text{WD}} = 10^{11}$ G and $B_{\text{WD}} = 3 \times 10^{10}$ G, respectively. All curves are calculated for a distance of 2 kpc.

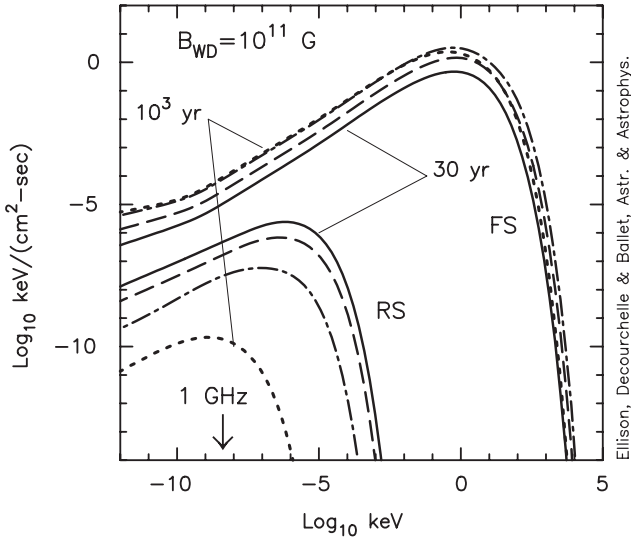


Fig. 8. Integrated synchrotron emission for a diluted ejecta magnetic field of $B_{\text{WD}} = 10^{11}$ G calculated at different ages: 30 yr (solid curves), 100 yr (dashed curves), 300 yr (dot-dashed curves) and 10^3 yr (dotted curves). The upper set of curves is from the forward shock and the lower set is from the reverse shock. Note that the dotted and dot-dashed curves for the FS almost overlay each other. The shock and SNR parameters are the same as in Fig. 7.

The evolution of the synchrotron emission is shown in Fig. 8 for our extreme diluted ejecta magnetic field $B_{\text{WD}} = 10^{11}$ G. The difference in radio emission at 1 GHz between the forward and reverse shocks is about a factor of 20 at 30 years and drops to more than five orders of magnitude at 1000 years, as shown in Fig. 7.

4.4. Heavy elements plasma

In the examples we have shown so far we considered only acceleration in fully ionized hydrogen. However, ejecta material is expected to be composed mainly of heavy elements and, in particular, type Ia supernovae are essentially devoid of hydrogen. There are two reasons for the acceleration process to be modified in the case of heavy elements.

First, the acceleration time and diffusion length depend on charge. For relativistic particles, the time required to accelerate an ion with charge $q = Ze$ to momentum p is proportional to $1/Z$. Likewise, the diffusion length of an ion with momentum p is proportional to $1/Z$ (e.g., Baring et al. 1999). Therefore, for given shock parameters, $p_{\text{max}} \propto Z$ regardless of whether p_{max} is determined by a finite shock age or size. A higher p_{max} tends to increase the acceleration efficiency if heavy ions are dominant compared to protons being dominant.

Second, a species with mass number A must have momentum $>Am_p c$ to be relativistic. Since p_{max} only increases as Z , this tends to result in a lower fraction of relativistic particles, and a γ closer to $5/3$, than in the case where protons are dominant. This tends to decrease the acceleration efficiency. In a mixed plasma containing light and heavy ions, the modified shock structure resulting from efficient DSA produces an additional effect whereby ions with the largest mass to charge ratio

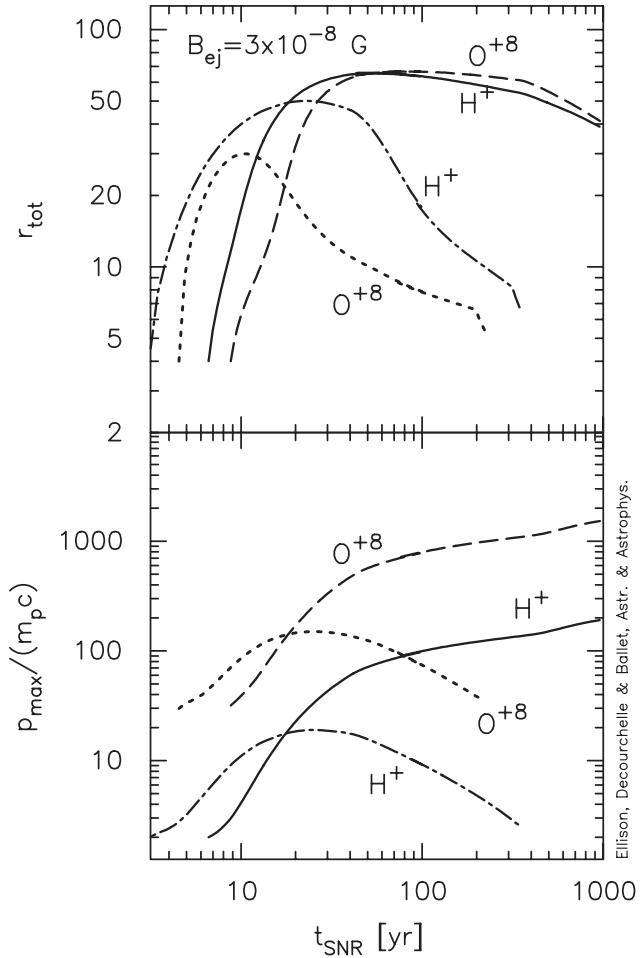


Fig. 9. Reverse shock r_{tot} 's and p_{max} 's for material containing only protons or fully ionized oxygen, as labeled. The ejecta magnetic field is taken to be constant at $B_{\text{ej}} = 3 \times 10^{-8}$ G in the solid and dashed curves, while a diluted field with $B_{\text{WD}} = 10^{11}$ G is used for the dot-dashed and dotted curves. Only results where $p_{\text{max}} > 2 Am_p c$ are shown.

are accelerated from thermal energies most efficiently. This is described in detail in Ellison et al. (1997) but is not considered here where we treat only single component plasmas.

In Fig. 9, using a constant $B_{\text{ej}} = 3 \times 10^{-8}$ G (solid and dashed curves) and our extreme white dwarf diluted field $B_{\text{WD}} = 10^{11}$ G (dot-dashed and dotted curves), we compare r_{tot} and p_{max} for a hydrogen plasma and for a fully ionized oxygen plasma. All other parameters are the same as those used for the examples shown in Fig. 3. For the constant $B_{\text{ej}} = 3 \times 10^{-8}$ G case, the difference in r_{tot} between protons and fully ionized oxygen becomes minor after ~ 50 yr. For the diluted magnetic field case, however, there are large differences in r_{tot} between the two species. The oxygen plasma shows a lower maximum r_{tot} peaking at an earlier age than the proton plasma. Based on this alone, whatever structural and temperature changes which occur in the interaction region are expected to be greater in hydrogen dominated type II supernovae envelopes than in heavy ion dominated type Ia supernovae.

5. Discussion

5.1. Observational evidence for DSA at reverse shocks

Projection effects and other problems make it difficult to reliably associate radio or X-ray nonthermal emission with reverse shocks in SNRs. Nevertheless, there have been recent claims for both.

Gotthelf et al. (2001) have identified the forward and reverse shocks in Cassiopeia A and showed that radio and Si emissivity radial profiles both show a sharp rise at what they characterize as the reverse shock. The sharp rise and fairly sharp falloff in radio emissivity as one moves outward from the center of the Cas A SNR is a good indication of the local acceleration of relativistic electrons, but, as noted, projection effects make the precise determination of the reverse shock difficult. Furthermore, Gotthelf et al. (2001) chose to ignore a secondary Si peak near 80 arcsec inside the main Si peak. The main Si peak seems clearly associated with radio emission, but the inner secondary peak is not and could alternately mark the reverse shock.

Using new VLA observations of Kepler's SNR, DeLaney et al. (2002) suggest that two distinct radio structures are present. These flat- and steep-spectrum components are partially decoupled in some areas and the steep-spectrum component tracks the X-ray emission seen by *ROSAT*, which is mainly line emission from shocked ejecta. They conclude that the flat- and steep-spectrum radio emission come from the forward and reverse shocks, respectively. However the steep regions could also mark the interface rather than the reverse shock. For example, Vink & Laming (2003) interpreted the (steep) radio emission from Cas A as arising at the interface.

Rho et al. (2002) claim that the detailed morphology of soft and hard X-rays in SNR RCW 86 strongly supports the case for different origins for these components. They conclude that the hard X-rays are most likely a combination of a synchrotron continuum plus Fe $K\alpha$ emission from shocked ejecta material. This implies, in their estimation, that the reverse shock may be accelerating electrons to energies of the order of 50 TeV!

While other interpretations are certainly possible, e.g., relativistic electrons produced at the forward shock might travel to the reverse shock and brighten in radio in the compressed magnetic field, the above observations provide some evidence that reverse shocks in SNRs can directly produce relativistic electrons; GeV in the case of radio and TeV in the case of nonthermal X-rays. If this is so, there are a number of important consequences both for interpreting a wide range of astrophysical sources where DSA is believed to generate relativistic electrons, and for our understanding of the basic functioning of DSA.

5.2. Implications

5.2.1. Magnetic field amplification

If relativistic electrons are accelerated at the reverse shock, the production of observable radio emission requires that the magnetic field upstream of the reverse shock be amplified by many orders of magnitude over values expected in the expanding

unshocked ejecta. If such field amplification is taking place, it is likely that it is directly associated with DSA (i.e., Bell & Lucek 2001).

We speculate that early in the SNR evolution (i.e., $t_{\text{SNR}} \lesssim 10$ yr) the unamplified ejecta field may be strong enough to start the DSA process even with dilution. Once energetic particles are produced, the magnetic field may be amplified by them and maintained against dilution at a level where DSA continues.

Shocks are widespread in astrophysics with parameters not widely different from those in SNRs. If DSA can amplify magnetic fields in SNR shocks, the process should work in other environments as well. Since the maximum energy individual particles obtain in DSA scales as B , widespread B -field amplification will lead to a systematic increase in the expected maximum proton energy produced by astrophysical shocks.

5.2.2. Extreme nonlinear effects

The theory of nonlinear diffusive shock acceleration predicts compression ratios far in excess of the test-particle value of $r_{\text{tot}} \approx 4$ (e.g., Eichler 1984; Ellison & Eichler 1984; Malkov 1998; Bell 1987; Berezhko & Ellison 1999; Blasi 2002). For high sonic Mach numbers, $M_S^2 > M_A$, and strongly modified steady-state conditions, the compression ratio can be approximated by $r_{\text{tot}} \sim 1.3 M_S^{3/4}$ or by $r_{\text{tot}} \sim 1.5 M_A^{3/8}$ when $M_S^2 < M_A$ (Kazanas & Ellison 1986; Berezhko & Ellison 1999).

We have shown that if B_{ej} falls in a range $3 \times 10^{-8} < B_{\text{ej}} < 3 \times 10^{-6}$ G with typical SNR parameters, $r_{\text{tot}} \sim 60$ may occur (see Fig. 3); a value considerably larger than is likely to occur in any other non-radiative astrophysical environment. Compression ratios this large should produce unmistakable changes in the SNR structure (see Figs. 4 and 6) and X-ray emission, thermal and nonthermal. Confirmation of this prediction would support the premise that DSA is intrinsically extremely efficient.

Unfortunately, shock compression ratios are not directly observable for remote systems such as SNRs with large Mach numbers (see Sects. 2.2.3.1 and 2.4 in Drury et al. 2001; Raymond 2001, respectively). Shocks in the heliosphere are directly observable but have low Mach numbers and even here, the direct measurement of compression ratios requires multiple spacecraft simultaneously sampling the upstream and downstream plasmas. Until the launch of CLUSTER this was not possible and the prediction of $r_{\text{tot}} > 4$ has not been clearly demonstrated in astrophysical shocks, although indirect support does exist for the Earth bow shock (Ellison et al. 1990).

The large structural changes brought about in SNRs if $r_{\text{tot}} \gg 4$ offer a unique opportunity to see the effects of extremely efficient diffusive shock acceleration. In the extreme cases we show here, i.e., Fig. 3, more than 90% of the bulk flow energy flux (in the shock rest frame) is placed in relativistic ions. Even in cases when r_{tot} is not as extreme, acceleration efficiencies near 50% are predicted for both the forward and reverse shocks. Over the lifetime of a SNR, $\sim 50\%$ of E_{SN} is predicted to be put into cosmic rays depending on the average injection rate over the surface of the SNR (e.g., Dorfi 1990; Berezhko et al. 1996, 2002; Ellison et al. 2004).

The energy which goes into relativistic ions comes out of the bulk thermal plasma and produces a drastic reduction in the shock temperature.

5.2.3. Cosmic-ray production

Direct observations of shocks in the heliosphere and most theories of DSA show that collisionless shocks put far more energy into ions than electrons. Thus, even though the presence of relativistic electrons suggested our description of strong nonlinear effects, the signature of nonlinear DSA in the structure and evolution of the radio and X-ray emitting interaction region between the forward and reverse shocks, will be evidence for the efficient production of cosmic-ray ions, not necessarily electrons (see Berezhko et al. 2003a, for a discussion of SN 1006 in this regard). Detection of pion-decay γ -rays would be a more direct confirmation that relativistic ions are produced in SNRs, however this has not yet been unambiguously done. It is also clear from γ -ray models of young SNRs, that parameters can be chosen where efficient DSA occurs, but either the γ -ray flux is below detectable levels, or detectable TeV γ -rays are dominated by inverse-Compton emission from electrons rather than protons (e.g., Ellison et al. 2001).

Modeling the SNR structure offers two advantages. First, if $r_{\text{tot}} > 4$ is inferred from observations, it is evidence for the efficient production of CR ions whether or not a pion-decay feature is observed since the observability of pion-decay γ -ray's depends on other factors besides acceleration efficiency (e.g., ambient density). Second, if the structure is inconsistent with efficient DSA and $r_{\text{tot}} \lesssim 4$, this is clear evidence that the efficient shock acceleration of ions is *not* occurring. Due to the freedom of γ -ray models, the lack of a γ -ray detection is unlikely ever to be able to eliminate the possibility that efficient DSA is occurring.

5.2.4. X-ray emission

For efficient particle acceleration, the postshock densities are larger and the postshock temperatures smaller than in the test-particle case (see Figs. 4 and 6). As a consequence, the heating of electrons in the downstream region by Coulomb interaction with the population of protons ($T_p \approx 1836 T_e$ without further heating at the shock) will be more efficient than in the test-particle case. In the shocked ejecta, the electron temperature can be almost equal to that of the protons for an injection of $\approx 10^{-2}$, while in the shocked ambient medium the electrons may reach up to 30% of the proton temperature (Decourchelle & Ellison 2001).

Another constraint on the efficiency of particle acceleration comes from the observation of a strong Fe K-alpha line in the shocked ejecta of young SNRs (like Cas A, Kepler and Tycho). In Kepler, for efficient particle acceleration at the reverse shock, it was shown that the shocked ejecta temperature gets too low to produce the Fe K-line (Decourchelle et al. 2000). Line excitation by the nonthermal population can be invoked, however the ionization state of iron is expected to be very low even when taking into account the ionization from a nonthermal

power-law population (Porquet et al. 2001). Thus, the prediction from efficient DSA that postshock temperatures are low in the RS presents a problem in SNRs where a strong Fe K-alpha line is observed.

5.2.5. Ionization fraction of ejecta material

For DSA acceleration to occur at all, the unshocked ejecta material must be fully ionized or, at least, have a sizable ionization fraction. Otherwise the magnetic turbulence necessary to scatter particles will be damped (e.g., Drury et al. 1996). The expanding ejecta will cool rapidly and would be largely neutral unless ionized by some source. This could possibly be X-ray emission from shock heated gas or the cosmic rays may contribute to the ionization themselves. If the ionization fraction is initially large enough for some cosmic-ray production to occur, these CRs may further ionize the precursor material, making acceleration more efficient, etc.

The Balmer-dominated spectra of nonradiative shocks in a number of SNRs (e.g., Ghavamian et al. 2001) has been interpreted as charge exchange between protons and neutrals. If synchrotron radio and/or X-ray emission is observed at these shocks as well, which is possibly the case in the northeastern rim of Tycho, this would indicate that DSA is at work even in a partially neutral medium. The reported presence of reverse shock radio emission suggests that the ejecta material is ionized, at least in the region upstream of the shock, where DSA is taking place.

6. Conclusions

It has long been believed that forward shocks in SNRs sweep up and accelerate ISM ions to produce galactic cosmic rays and to accelerate electrons to produce in situ radio emission. The mechanism most likely responsible for this is DSA, which is predicted to be extremely efficient, i.e., >50% of the ram kinetic energy may go into relativistic ions. At reverse shocks in young SNRs, however, straightforward estimates of the diluted ejecta magnetic field from the pre-SN white dwarf or massive star show it to be many orders of magnitude below that required to either accelerate relativistic electrons from the thermal background, or to produce observable radio intensities from background cosmic-ray electrons.

Nevertheless, some recent observations provide evidence for radio emission associated with reverse shocks in two SNRs: Kepler and Cas A, and X-ray synchrotron continuum emission in RCW 86. If the reverse shocks in these remnants are accelerating electrons to GeV or even TeV energies via DSA, it immediately suggests that the magnetic field at the reverse shock is orders of magnitude higher than expected to produce radio and higher still to produce X-ray synchrotron. If true, the most likely explanation is that the acceleration process is amplifying the magnetic field, perhaps as Bell & Lucek (2001) have suggested. The importance of shock acceleration in a wide variety of astrophysical objects, and the strong dependence of DSA on the magnetic field, make it critically important to first, verify the difficult reverse shock observations and second,

to explore the ramifications of efficient DSA at reverse shocks in young SNRs.

While radio observations imply magnetic field amplification to values far larger than the diluted progenitor field, there is, as yet, no way to precisely determine the value. This opens the possibility that the ejecta field B_{ej} is large enough to produce observable radio emission, but still far lower than normal ISM values. We have shown here that, for typical SNR parameters, having $3 \times 10^{-8} < B_{ej} < 3 \times 10^{-6}$ G results in extremely large nonlinear effects in DSA, i.e., compression ratios $\gg 4$ and shocked temperatures \ll than test-particle temperatures. If these nonlinear effects occur, they will produce large changes in the structure and evolution of SNRs which should be observable with existing instruments. We have detailed these effects in the remnant hydrodynamics and estimated synchrotron emission for a limited range of parameters.

Supernova remnants may offer the best known laboratory for studying both magnetic-field amplification and DSA. Current and future ground and space-based observatories offer high spatial and energy resolution of several remnants and provide information that is available nowhere else. Shocks in the Heliosphere are accessible to spacecraft and a great deal has been learned of their properties. However, the point-like nature of heliospheric observations, the low Mach number and small size of heliospheric shocks which limits particle acceleration, and the unique geometry of the intensely studied Earth bow shock, limit what can be learned and transferred to other astrophysical systems. The difficult plasma physics has also limited the success of analytic investigations, and direct PIC computer simulations are decades away from being able to simulate the injection and acceleration of a electron-proton plasma to relativistic energies.

Acknowledgements. The authors wish to thank J. Blondin for providing his hydrodynamic simulation code *VH-1* and for other help with this project. We are also grateful to the International Space Science Institute (ISSI) in Bern, Switzerland, where some of this work was done. This work was supported, in part, by a NSF-CNRS grant (NSF INT-0128883, CNRS-12974) and by an NASA ATP grant (ATP02-0042-0006).

References

- Baring, M. G., Ellison, D. C., Reynolds, S. P., Grenier, I. A., & Goret, P. 1999, *ApJ*, 513, 311
- Bell, A. R. 1987, *MNRAS*, 225, 615
- Bell, A. R., & Lucek, S. G. 2001, *MNRAS*, 321, 433
- Berezhko, E. G. 1996, *Astropart. Phys.*, 5, 367
- Berezhko, E. G., & Ellison, D. C. 1999, *ApJ*, 526, 385
- Berezhko, E. G., Elshin, V. K., & Ksenofontov, L. T. 1996, *JETP*, 82, 1
- Berezhko, E. G., Ksenofontov, L. T., & Völk, H. J. 2002, *A&A*, 395, 943
- Berezhko, E. G., Ksenofontov, L. T., & Völk, H. J. 2003, *A&A*, 412, L11
- Berezhko, E. G., Pühlhofer, G., & Völk, H. J. 2003, *A&A*, 400, 971
- Berezhko, E. G., & Völk, H. J. 2004, *A&A*, 419, L27
- Blasi, P. 2002, *Astropart. Phys.*, 16, 429
- Decourchelle, A., & Ellison, D. C. 2001, *Space Sci. Rev.*, 99, 219
- Decourchelle, A., Ellison, D. C., & Ballet, J. 2000, *ApJ*, 543, L57
- DeLaney, T., Koralesky, B., & Rudnick, L. 2002, *ApJ*, 580, 914
- Dorfi, E. A. 1990, *A&A*, 234, 419
- Drury, L. O'C. 1983, *Rep. Prog. Phys.*, 46, 973
- Drury, O. C., Duffy, P., & Kirk, J. G. 1996, *A&A*, 309, 1002
- Drury, L. O'C., Ellison, D. C., Aharonian, F. A., et al. 2001, *Space Sci. Rev.*, 99, 329
- Drury, L. O'C., van der Swaluw, E., & Carroll, O. 2003 [[arXiv:astro-ph/0309820](https://arxiv.org/abs/astro-ph/0309820)]
- Eichler, D. 1984, *ApJ*, 277, 429
- Ellison, D. C., Berezhko, E. G., & Baring, M. G. 2000, *ApJ*, 540, 292
- Ellison, D. C., Decourchelle, A., & Ballet, J. 2004, *A&A*, 413, 189
- Ellison, D. E., Drury, L. O'C., & Meyer, J.-P. 1997, *ApJ*, 487, 197
- Ellison, D. C., & Eichler, D. 1984, *ApJ*, 286, 691
- Ellison, D. C., Möbius, E., & Paschmann, G. 1990, *ApJ*, 352, 376
- Ellison, D. C., Slane, P., & Gaensler, B. M. 2001, *ApJ*, 563, 191
- Ghavamian, P., Raymond, J., Smith, R. C., & Hartigan, P. 2001, *ApJ*, 547, 995
- Gotthelf, E. V., Koralesky, B., Rudnick, L., et al. 2001, *ApJ*, 552, L39
- Jones, F. C., & Ellison, D. C. 1991, *Space Sci. Rev.*, 58, 259
- Kazanas, D., & Ellison, D. C. 1986, *ApJ*, 304, 178
- Liebert, J. 1995, in *Cape Workshop on Magnetic Cataclysmic Variables*, ed. D. A. H. Buckley, & B. Warner (San Francisco: ASP), ASP Conf., 85, 59
- Lucek, S. G., & Bell, A. R. 2000, *MNRAS*, 314, 65
- Malkov, M. A. 1998, *Phys. Rev. E*, 58, 4911
- Porquet, D., Arnaud, M., & Decourchelle, A. 2001, *A&A*, 373, 1110
- Ptuskin, V. S., & Zirakashvili, V. N. 2003, *A&A*, 403, 1
- Raymond, J. 2001, *Space Sci. Rev.*, 99, 209
- Rho, J., Dyer, K. K., Borkowski, K., & Reynolds, S. P. 2002, *ApJ*, 581, 1116
- Ruiz-Lapuente, P., & Spruit, H. C. 1998, *ApJ*, 500, 360
- Rybicki, G. B., & Lightman, A. P. 1979, *Radiative Processes in Astrophysics* (John Wiley & Sons), 171
- Vink, J., & Laming, J. M. 2003, *ApJ*, 584, 758
- Völk, H. J., Berezhko, E. G., Ksenofontov, L. T., & Rowell, G. P. 2002, *A&A*, 396, 649